Nanoscale

Cite this: *Nanoscale*, 2012, **4**, 6461

www.rsc.org/nanoscale

PAPER

Selective deposition of Pt onto supported metal clusters for fuel cell electrocatalysts†

Tae-Yeol Jeon,[a] Nicola Pinna,[ab] Sung Jong Yoo,[c] Docheon Ahn,[d] Sun Hee Choi,[d] Marc-Georg Willinger,[e] Yong-Hun Cho,[f] Kug-Seung Lee,[a] Hee-Young Park,[c] Seung-Ho Yu[a] and Yung-Eun Sung*[a]

Received 12th July 2012, Accepted 15th August 2012
DOI: 10.1039/c2nr31819a

We report a new method for deposition of Pt on a metal core to develop real electrocatalysts with significantly reduced amounts of expensive Pt as well as enhanced activity for oxygen reduction reaction. Ru and Pd have different crystal structures and modify the electronic structure of Pt to a different extent (shifts in d-band center). They were chosen as core materials to examine whether hydroquinone dissolved in ethanol can be used to deposit additional Pt atoms onto preformed core nanoparticles, and whether the modified d-character of Pt on different host metals can result in the enhanced ORR activity. The physicochemical characteristics of Pd–Pt and Ru–Pt core–shell nanoparticles are investigated. The core–shell structure was identified through a combination of experimental methods, employing electron microscopy, electrochemical measurements, and synchrotron X-ray measurements such as powder X-ray diffraction, X-ray absorption fine structure, and X-ray photoelectron spectroscopy. The hydroquinone reduction method proved to be an excellent route for the epitaxial growth of a Pt shell on the metal cores, leading to enhanced ORR activities.

Introduction

Heteronuclear metal–metal bonds formed by alloying different metals have been extensively studied because they influence the electronic, chemical, and catalytic properties of metals.[1,2] For electrocatalysis such as the oxygen reduction reaction (ORR),[3,4] which limits the overall efficiency of proton exchange membrane fuel cells (PEMFCs) due to its sluggish kinetics and the dissolution of metal catalysts under the ORR operating conditions,[5–7] the formation of a Pt shell can significantly contribute to the improvement of the utilization of Pt and the activity and stability of electrocatalysts can be maximized by controlling the thickness of the Pt shell[8] and by selecting an appropriate substrate.[4,9–11] Nørskov *et al.* performed theoretical calculations on the ORR[12–14] and clearly demonstrated its origin as well as trends in the activities and the stabilities of Pt- and Pd-based transition metal alloys.[4,7,15]

Alloying can be the most efficient method for modifying the valence band structure of surface Pt atoms, as discussed by Hammer and Nørskov.[13] Among the Pt-based alloy systems, model studies and their corresponding experimental results suggest several candidates (Pt/Pd(111), Pt_3Ni, Pt_3Y, and Pt_3Sc), which are generally accepted as promising ORR catalysts that are both active and kinetically stable under the ORR operating conditions.[2,4] Keeping in mind the theoretical advancements, new methods for the preparation of core–shell nanoparticles with a monolayer-level Pt shell are truly required to produce the best practical fuel cell electrocatalysts that have been predicted by theoretical studies.

Based on the d-band model, Pt atoms deposited on the surface of host metals such as Pd and Ru exhibit a downshift of the d-band center relative to that of pure Pt.[4] Moreover, the binding energies of important oxygen-containing species such as O, OH and OOH, which are in the scaling relations of adsorption energy,[16,17] also decrease. Among the various precious metals, Pd as a host has shown the highest activity. On the other hand, Ru has not been chosen as the core material due to an excessively large downshift of the d-band center position in Ru–Pt core–shell

[a]*World Class University (WCU) program of Chemical Convergence for Energy & Environment (C_2E_2), School of Chemical and Biological Engineering, College of Engineering, Seoul National University (SNU), Seoul, Korea. E-mail: ysung@snu.ac.kr*
[b]*Department of Chemistry, CICECO, University of Aveiro, 3810-193 Aveiro, Portugal*
[c]*Fuel Cell Center, Korea Institute of Science and Technology, Seoul 136-791, Korea*
[d]*Pohang Accelerator Laboratory, Pohang University of Science and Technology, Pohang 790-784, Korea*
[e]*Department of Inorganic Chemistry, Fritz-Haber-Institut of the Max-Planck Society, Faradayweg 4-6, 14195 Berlin, Germany*
[f]*School of Advanced Materials Engineering, Kookmin University, Seoul 136-702, Korea*

† Electronic supplementary information (ESI) available: Atomic ratio of Pt to Pd of Pt[0.5]/Pd/C obtained from energy-dispersive X-ray spectroscopy (EDS). TEM images of as-prepared Ru/C and Pd/C. TEM images and particle size distribution histograms of Pd/C, Pt[0.1]/Pd/C, Pt[0.3]/Pd/C, and Pt[0.5]/Pd/C. ORR currents of Pt[0.2–1.4]/Ru/C and Pt[0.1–0.7]/Pd/C. Refined lattice parameters of Ru–Pt core–shell nanoparticles from powder X-ray diffraction. Detailed EXAFS parameters of Pd– and Ru–Pt core–shell nanoparticles. See DOI: 10.1039/c2nr31819a

structures.[4] However, Pd and Ru have different crystal structures, *i.e.*, face-centered cubic (fcc) and hexagonal closed-packed (hcp), respectively. Pt overlayers on these two metals present an ideal case to study electronic and geometric characteristics of Pt-based alloy nanoparticles with a core–shell architecture.

In general, a Pt overlayer can be formed on the surface of a metal core by slow reduction using weak reducing agents,[18–22] according to a mechanism explained by the growth model proposed by LaMer and Dinegar.[23] While the formation of isolated Pt nuclei is energetically unfavorable, diffusion-controlled atom addition can occur on the primary particles at an early stage. Typically, a Pt overlayer for the electrocatalysts in fuel cells can be formed on precious metal cores by a Cu-underpotential deposition-mediated electrodeposition method.[8] It allows controlling the rate of Pt deposition by cycling between the bulk deposition potentials of Cu and Pt resulting in the formation of smooth Pt shells. Surprisingly, the redox behavior of hydroquinone/quinone (HQ/Q) has not yet been systematically applied to the reduction of precious metals except for Ag and Au.[24,25] HQ has not only been considered as the principal chemical reducing agent to grow Ag on a substrate, but also as a model redox system for achieving fundamental understanding of organic redox reactions that have been implicated in biological electron transport processes. Recently, it has been reported that the HQ/Q system has a complete 3×3 array of redox species in its reaction pathways, which are mainly dependent on environmental factors such as the solvent.[26] Peover has already shown that the redox behavior of quinones in water is significantly different from that in aprotic solvents such as acetonitrile due to the capacity of water for hydrogen bonding, which results in the stabilization of the anions and, therefore, increases the redox potential of HQ/Q.[27] Gupta and Linschitz have shown that the first and second redox peaks shift to the positive direction in potentials with similar reversibilities when various alcohols are added to aprotic solvents.[28] They also examined alcohols with higher pK_a than that of the corresponding quinone in order to eliminate the possibility of protonation from alcohols; they revealed that the redox behavior of quinone primarily depends on the degree of hydrogen-bonding interactions. Quan *et al.* reported a two-electron redox process;[26] they examined the cyclic voltammetry of HQ in unbuffered and buffered aqueous solutions, when HQ underwent a two-electron oxidation. In a buffered solution with pH = 7, quinone is primarily reduced to the H_2Q form, whereas in an unbuffered neutral solution, the amount of other reduced forms is determined by the pK_a values of the quinone-derivatives and solvent.

In this work, we report a new approach that applies the redox chemistry of HQ/Q in a protic solvent[29] for the selective deposition of Pt overlayers onto Pd and Ru nanoparticles. HQ in our synthetic system follows a two-electron redox process. The core–shell nanocatalysts prepared by the HQ reduction method were examined using high resolution-transmission electron microscopy (HR-TEM) and various synchrotron X-ray techniques such as powder X-ray diffraction (PXRD), X-ray absorption fine structure (XAFS), and X-ray photoelectron spectroscopy (XPS). Finally, the electrochemical properties of the core–shell nanoparticles were further examined by oxygen reduction activity and cyclic voltammetry.

Experimental

Chemicals and materials

All chemicals are Aldrich products, except for oleylamine ($C_{18}H_{35}NH_2$, >40%, TCI); ruthenium(III) chloride hydrate ($RuCl_3 \cdot xH_2O$, 99.98%), palladium(II) acetylacetonate ($Pd(C_5H_7O_2)_2$, 99%), platinum(IV) chloride ($PtCl_4$, 99.9+%), anhydrous ethanol (C_2H_6O, 99.5%), 1,2-propanediol ($C_3H_8O_2$, 99.5%), sodium borohydride ($NaBH_4$, 99%), and hydroquinone ($C_6H_6O_2$, 99%).

Preparation of Ru/C and Pd/C

Ru/C (21.1 wt%) was prepared *via* a borohydride reduction method in anhydrous ethanol. 0.25 mmol (0.08 mL) oleylamine was added to anhydrous ethanol (200 mL), and stirred for 30 min. 0.15 g of Vulcan XC-72R was added to the solution and dispersed by sonication for 40 min. After additional stirring for 30 min, ruthenium(III) chloride hydrate (0.1024 g) dissolved in anhydrous ethanol (60 mL) was added and stirred for 12 h. After sonication for 3 min, 0.49 mmol of $NaBH_4$ dissolved in 20 mL of anhydrous ethanol was quickly added to the ruthenium solution under vigorous stirring. The solution (280 mL) was stirred for 6 h, followed by filtration, washing with ethanol and drying in a vacuum oven at 40 °C.

Pd/C (28.4 wt%) was prepared through a similar process to the synthesis of Ru/C with the exception of using 1,2-propanediol as a solvent. Palladium(II) acetylacetonate (0.1718 g) was dissolved in 80 mL of 1,2-propanediol. This precursor solution was added to a solution composed of 1.58 mmol (0.36 mL) oleylamine, 100 mL of 1,2-propanediol, and 0.15 g of Vulcan XC-72R. This mixture solution was stirred for 12 h. After sonication for *ca.* 5 min, the solution was heated to 110 °C under an Ar flow and maintained at this temperature for 1 h to remove residual water. After that, 0.30 mmol of $NaBH_4$ dissolved in 20 mL of 1,2-propanediol was quickly added to the solution under vigorous stirring and maintained at this temperature for 2 h. The filtering, washing, and drying were carried out as for the Ru/C process.

A heat-treatment was carried out on dried Ru/C and Pd/C samples in order to modify the particle size and to remove impurities such as dissolved carbons in the Pd lattice.[30–32] The Ru/C was heat-treated for 1 h at 300 °C under Ar. For Pd/C the sample was heated to 200 °C in dry synthetic air and held at 200 °C for 1 h before being held at 200 °C for 5 min under Ar and an additional hour under Ar–H_2 (5 vol%) prior to being cooled to RT under Ar.

Pt deposition on carbon-supported metal nanoparticles

Pt deposition on the surface of the metal nanoparticles follows the same procedure as on Pd/C and Ru/C nanostructures. An appropriate amount (0.08–0.2 g) of Ru/C (or Pd/C) was dispersed in 100 mL of anhydrous ethanol and sonicated for 10 min. After additional stirring for 10 min, platinum(IV) chloride and HQ (molar ratio of HQ : $PtCl_4$ = 20 : 1) dissolved in 60 and 40 mL of anhydrous ethanol, respectively, were added to the solution containing the core materials. This solution was stirred for 1 h. After a final sonication for only 3 min, in order to avoid the reduction of Pt ions, the solution was loaded into a three-

neck flask. The solution was then deaerated under Ar, heated to 70 °C at the rate of *ca.* 1.25 °C min^{-1} and kept for 2 h at this temperature. The solution was then cooled, filtered, washed with ethanol at room temperature, and dried at 40 °C in a vacuum oven.

A control experiment was also performed by replacing Pd/C and Ru/C nanostructures by carbon black. An appropriate amount of HQ (molar ratio of HQ : $PtCl_4$ = 20 : 1) was dissolved in a dispersion of carbon black (Vulcan XC-72R) in ethanol. To this solution an ethanol solution of platinum(IV) chloride (0.0572 g) was added. After stirring for 1 h, the solution was heated under the same conditions as for the preparation of the core–shell samples.

Characterization

ICP-AES elemental analyses were performed with an Optima-4300 DV (Perkin-Elmer) spectrometer. Transmission electron microscopy (TEM) investigations were carried out using a Philips CM200 FEG and a JEOL 2010 both operating at 200 kV. Samples for TEM investigations were prepared by first dispersing the particles in ethanol under the assistance of ultrasonication and then dropping one drop of the suspension on a copper TEM grid coated with a holey carbon film. Powder X-ray diffraction (PXRD) data were measured at the 8C2 high-resolution powder diffraction beamline of Pohang Accelerator Laboratory (PAL). For the XRD, the incident X-rays were vertically collimated by a mirror, and monochromatized to the wavelength of 1.5490 Å using a double-crystal Si(111) monochromator. The detector arm of the vertical scan diffractometer is composed of seven sets of Soller slits, flat Ge(111) crystal analyzers, anti-scatter baffles, and scintillation detectors, with each set separated by 20°. Each specimen of *ca.* 0.2 g powder was prepared by a flat plate side loading method to avoid preferred orientation, and the sample was then rotated about the normal to the surface during the measurement in order to increase sampling statistics. A step scan was performed at room temperature from 10° in 2θ with 0.02° increments and 1° overlaps to the next detector bank up to 131° in 2θ. In order to determine accurately the lattice parameters of the phases in the prepared samples, synchrotron powder XRD patterns were fitted with a whole-pattern profile matching method, modeling the system as multi-phases.[33] The procedure for the fitting is as follows. The lattice parameters of Ru and C in the composite of Ru/C are determined at first from whole-pattern profile matching for the XRD pattern. The given lattice parameters of Ru and C were fixed and then the lattice parameters of Pt in the composites of Pt/Ru/C were fitted using whole-pattern profile matching for the XRD patterns.

X-ray absorption fine structure (XAFS) experiments were conducted on beamline 5A of PAL (2.5 GeV; 150–180 mA). The incident beam was monochromatized using a Si(111) double crystal monochromator and detuned by 30% to minimize the contamination from higher harmonics, in particular, the third order reflection of the silicon crystals. The spectra for L_{III}-edge of Pt (E_0 = 11 564 eV) were taken in a transmission mode with separate He-filled IC Spec ionization chambers for incident and transmitted beams, respectively. Before measuring the samples, energy was calibrated by using a Pt foil. The energy scan was performed in five regions for good energy resolution in a steep absorption and measurement of XANES and EXAFS spectra at a time, using 5 eV-steps in the region of 11 364–11 514 eV, 1 eV-steps in 11 514–11 554 eV, 0.25 eV-steps in 11 554–11 594 eV, 0.03 *k*-steps in 11 594–12 104 eV, and 0.04 *k*-steps in 12 104–12 564 eV. The obtained data were processed in the usual way to obtain the absorbance and analyzed with ATHENA and ARTEMIS in the suite of IFEFFIT software programs.[34] Pre-edge absorption due to the background and detector was subtracted using a linear fit to the data in the range of −200 to −60 eV relative to E_0. E_0 was defined as the first inflection point on the rising absorption edge. Each spectrum was then normalized by a constant, an extrapolated value to E_0 of the third-order polynomial fit over absorption at 150–900 eV relative to E_0. To isolate the EXAFS signal, the post-edge background function was approximated with a piecewise spline that could be adjusted so that the low-*R* component of pre-Fourier transformed data was minimized. After calculation of EXAFS function $\chi(k)$, k^3-weighted EXAFS function in momentum (k) space was Fourier transformed to reveal the neighboring atoms arranged according to the distance from a central atom in *R*-space. The *k* range of the transform varied between a k_{min} of 2.0–3.0 $Å^{-1}$ and a k_{max} of 12.0–13.0 $Å^{-1}$. The Kaiser–Bessel function was adopted as a window function and the windowsill of dk = 1.5 was also used in the transform. A shell of interest in *R*-space was back-transformed into the momentum space with the Kaiser–Bessel window function and a windowsill of dR = 0.1. Fourier-filtered spectra derived from the experiments were fitted by using the theoretical standards generated with the *ab initio* FEFF 8.2 code.[35] The standard Pt–O and Pt–Pt phase-shift and amplitude functions were extracted from the structures of β-PtO_2 (ref. 36) and Pt metal,[37] respectively. The standard Pt–Pd functions were produced by using the structure of Pt metal with Pd atoms replaced at the nearest neighboring Pt positions.

X-ray photoelectron spectroscopy (XPS) measurements were performed on the soft X-ray beam line (8A1) connected to an undulator (U7) at PAL. The end station was composed of a high performance electron analyzer (SCIENTA-200) with energy and angular resolution of 5 meV and 0.5°, respectively. The experiment was carried out in an ultrahigh vacuum (UHV) chamber with a base pressure $\leq 5 \times 10^{-10}$ Torr. All spectra were measured using 630 eV of incident photon energy. The Shirley background is subtracted from the measured spectra. The position of the center of the valence band is given by the following equation:

$$\int N(\varepsilon)\varepsilon d\varepsilon / \int N(\varepsilon) d\varepsilon \quad (1)$$

where $N(\varepsilon)$ is the DOS[3,38] or, in our case, the XPS-intensity after background subtraction. The background-subtracted spectra were integrated up to 10.0 eV BE with respect to E_F, which is calculated from the Au film as a reference.

Electrochemical measurements

A catalyst ink slurry was prepared by mixing 0.01 g of electrocatalysts with 20 μL of distilled (DI) water, 800 μL of isopropyl alcohol (IPA), and 57.2 μL of 5 wt% Nafion solution. After ultrasonication, 7 μL of the ink slurry was pipetted onto a glassy carbon substrate (the geometric surface areas for CVs and RDE

are 0.283 cm^2 and 0.196 cm^2, respectively). Electrochemical measurements were conducted using an Autolab potentiostat (PGSTAT128N) in a standard three-compartment electrochemical cell with a glassy carbon electrode (Sigradur, HTW Germany), Pt wire, and saturated calomel electrode (SCE) as working, counter, and reference electrodes, respectively. All the potentials except for ORR polarization curves were quoted with respect to the normal hydrogen electrode (NHE), and measurements were conducted at 293 K using a thermostat. ORR polarization curves were obtained by scanning from −0.094 to 0.756 V *vs.* SCE in a 0.1 M $HClO_4$ solution under an O_2 flow using a rotating-disk electrode (RDE) at a rotation rate of 1600 rpm and scan rate of 5 mV s^{-1}; the forward sweep of the first cycle is displayed in Fig. 6a. The currents of the Pt RDE in H_2-saturated 0.1 M $HClO_4$ solution were zero at −0.293 V *vs.* SCE. Hence, the obtained data were shifted by +0.293 V and the potentials are quoted on the RHE scale.

To calculate the kinetic current density based on ORR polarization curves, the Koutecky–Levich equation was applied as follows:

$$\frac{1}{i} = \frac{1}{i_d} + \frac{1}{i_k} \quad (2)$$

where, i is the measured current, i_d is the diffusion (mass-transfer) limited current, and i_k is the kinetic limit of the current. Thus, i_k can be calculated from the following equation:

$$i_k = \frac{i \times i_d}{i_d - i} \quad (3)$$

The mass-specific kinetic current at 0.9 V *vs.* RHE (*cf.* Fig. 6b) was obtained by normalizing the currents of each sample with loading amounts of total metal and Pt.

Results and discussion

Synthesis and characterization

The carbon-supported Ru (21.1 wt%) and Pd (28.4 wt%) nanoparticles were prepared using the borohydride reduction method in ethanol and 1,2-propanediol, respectively. Fig. S2a and b† show the TEM images of as-prepared pure Ru and Pd supported on carbon black (see the ESI†). The TEM images of the heat-treated Ru/C and Pd/C nanostructures show that the metal nanoparticles (dark dots) are well dispersed onto the carbon black (grey particles of *circa* 100 nm in size) (Fig. 1a and c). The metal nanoparticles are relatively homogeneous in size and predominantly present a spherical shape. The morphological aspects of the Ru/C and Pd/C nanostructures are highly desirable for the uniform deposition of Pt carried out in the second step. To prepare Ru–Pt and Pd–Pt core–shell nanoparticles, we modified a typical seed-mediated growth method,[39] based on the aforementioned HQ oxidation reaction in ethanol at 70 °C.[29]

The particle size distribution was obtained by counting 100 particles from overview TEM images including the ones shown in Fig. 1a–d prior to and after Pt deposition (Fig. 1e and f). The average particle size of both Ru and Pd clusters increases upon Pt deposition, suggesting that Pt is deposited onto the metal clusters. As a matter of fact, metal clusters in the Ru/C and Pd/C samples have average diameters of 3.4 and 5.6 nm, respectively

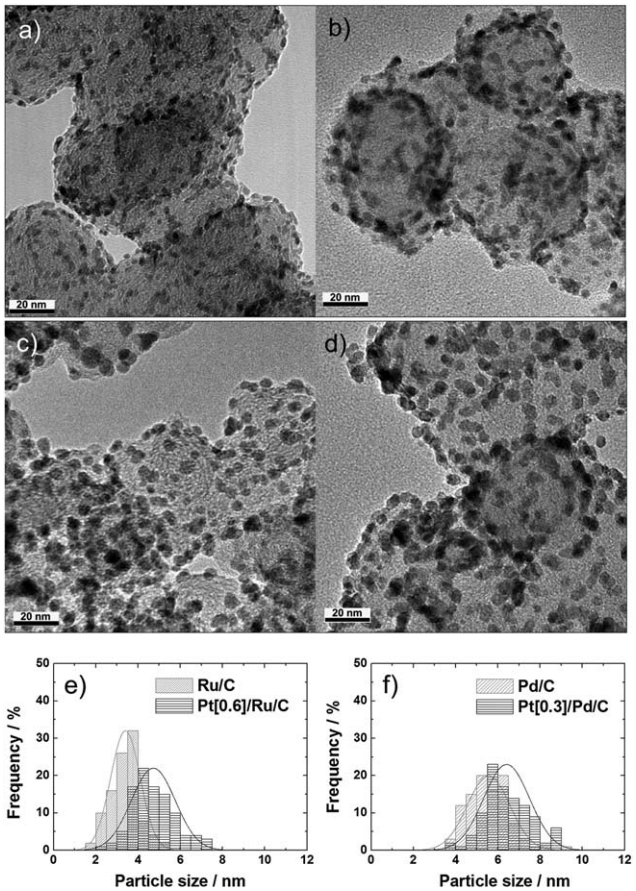

Fig. 1 TEM images of heat-treated core and core–shell nanoparticles. (a) Ru/C (21.1 wt%) and (b) Pt[0.6]/Ru/C have the average particle diameters of 3.4 and 4.7 nm, respectively. (c) Pd/C (28.4 wt%) and (d) Pt[0.3]/Pd/C, 5.6 and 6.4 nm, respectively. Particle size distribution histograms of carbon-supported (e) Ru, Pt[0.6]/Ru, and (f) Pd, Pt[0.3]/Pd nanoparticles.

(Fig. 1a and c). Whereas, after Pt deposition, the metal clusters in the Pt[0.6]/Ru/C and Pt[0.3]/Pd/C samples (atomic ratios of Pt : Ru and Pt : Pd = 0.37 : 0.63 and 0.23 : 0.77, respectively) have larger average particle sizes of 4.7 and 6.4 nm, respectively (Fig. 1b and d). The amount of Pt needed to increase the size of the particles from 5.6 to 6.4 corresponds to the total amount of Pt added to the reaction mixture. This indicates that (almost) all the additional Pt atoms are deposited onto the surface of the Pd and Ru nanoparticles. The TEM images and particle size distribution histograms of pure Pd, Pd[0.1]/Pd, Pt[0.3]/Pd, and Pt[0.5]/Pd supported on carbon black can be seen in Fig. S3.†

Fig. 2 shows the results of HRTEM studies performed on the Pd/C (a and b) and Pt[0.5]/Pd/C (c) catalysts. The HRTEM image presented in Fig. 2a, with the corresponding power spectrum in the inset, is characteristic of a Pd particle oriented along the [110] direction.

The image shown in Fig. 2b is characteristic of a twinned particle oriented along the [110] direction. The sharp reflection marked (1) belongs to the 111-family of the two twins. The reflections (3) and (4) belong to the 111-family of the left and right part of the particle, respectively. Finally, the reflections (2) and (5) belong to the 200-family of the left and right twin,

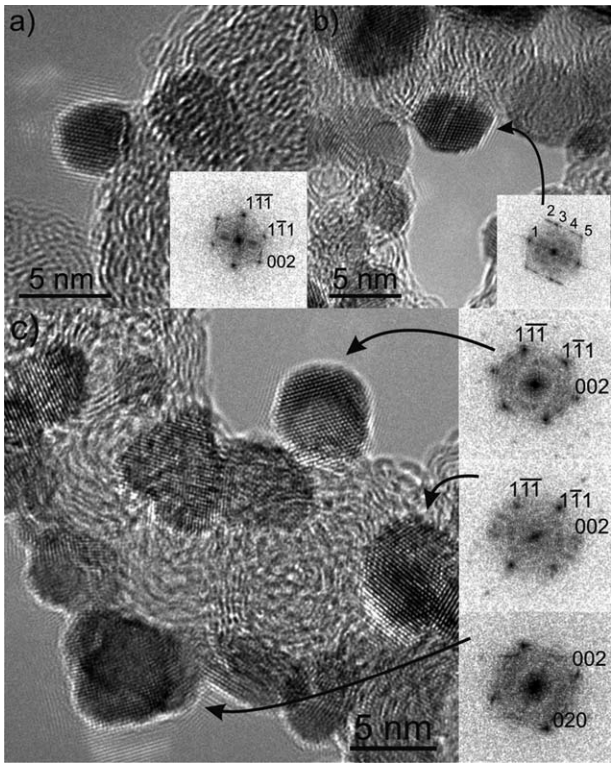

Fig. 2 (a and b) High resolution TEM images of the supported Pd nanoparticles in the Pd/C sample and in the insets are power spectra of two selected nanoparticles (indicated by arrows). (c) High resolution TEM image of the supported Pd–Pt core–shell nanoparticles in the Pt [0.5]/Pd/C.

respectively. After Pt deposition, the nanoparticles on the carbon black not only become slightly larger than in the case of the pure Pd/C samples, but, remarkably, also show a change in morphology. The Pt deposition process induces a transition from spherical to more irregular shapes as shown in Fig. 2c. The power spectra of three selected nanoparticles are characteristics of single crystalline Pt and Pd nanoparticles oriented along the [110] (top and middle insets) and [100] (bottom inset) directions, respectively. These findings suggest that Pt is epitaxially deposited onto the preformed Pd nanoparticles.

The chemical analysis of core–shell nanoparticles was performed by inductively coupled plasma-atomic emission spectroscopy (ICP-AES). The results for Ru–Pt and Pd–Pt core–shell particles are in good agreement with the nominal values (Table 1). ICP-AES data demonstrate that the HQ reduction method leads to the controlled deposition of Pt and, at the same time, has no effect on the dissolution of core materials. These ICP-AES results were used as metal loadings in order to evaluate the accurate mass-specific ORR activity (*cf.* Fig. 6b).

Synchrotron powder X-ray diffraction (PXRD) analysis was performed in order to examine the structural characteristics of metal nanoparticles in the Ru–Pt (Fig. 3a and b) and Pd–Pt (Fig. 3c) samples. The peaks centered at $2\theta \sim 25°$ in Fig. 3a and b are due to the carbon support. The other peaks for the Ru/C sample are characteristics of hexagonal close packed (hcp) ruthenium (JCPDS card no. 6-663). It is noteworthy that the main structures in the patterns of Ru–Pt are still due to the Ru phase even at high Pt loading (Pt[1.4] in Fig. 3a). Additional broad peaks around the diffraction angles of face-centered cubic (fcc) platinum (JCPDS card no. 4-802) are observed. The contribution of the Pt(111) peak (around $2\theta \sim 40°$) became clear with the increase of the Pt content, accounting for the nonsymmetrical shape[43] of the Ru peaks around the diffraction angles of Pt. In order to accurately determine the lattice parameters (Table S1†) of Pt in the surface layer of Ru–Pt, synchrotron powder XRD patterns were fitted using a whole-pattern profile matching method.[33] As the Pt loading increases the lattice parameter of Pt obtained from the fit increases from 3.84 Å for Pt[0.6]/Ru/C to 3.90 Å for Pt[1.6]/Ru/C approaching the value of pure Pt (3.92 Å) (Fig. 3b). This implies that as the Pt loading increases, the effect of Ru substrate on the contraction of the Pt lattice parameter becomes weaker. In the case of Pd–Pt (Fig. 3c), however, the strain effect could not be observed from the XRD patterns due to the same crystal structure (fcc) and similar lattice parameters. In contrast, the Pt–Pt distances of Pd–Pt and Ru–Pt core–shell nanoparticles from the extended X-ray absorption fine structure (EXAFS) confirmed contraction of Pt overlayers, *i.e.*, decrease of the interatomic distance.

Additional structural information on the Pd–Pt and Ru–Pt core–shell nanoparticles was extracted from the EXAFS. The Fourier transformed k^3-weighted EXAFS at the Pt L_{III} edge for commercial Pt, Pd–Pt (Fig. 3d, right) and Ru–Pt (Fig. 3d, left) were plotted as a radial structure function (RSF) without phase shift correction. The structural parameters for the Pd–Pt and Ru–Pt core–shell nanoparticles obtained from EXAFS data analysis are shown in Table 2, respectively. The detailed EXAFS parameters for the Pd–Pt and Ru–Pt can be also found in Tables S2 and S3,† respectively. The Pt–Pt distances (R) in the core–shell nanoparticles are smaller than that of commercial pure Pt due to compressive strains that result from the interaction of Pt overlayer with Pd and Ru substrates. In addition, the RSF peak at ~2.7 Å, which is the main Pt–Pt scattering, becomes apparent for Pt[1.4]/Ru and Pt[0.7]/Pd only. These results suggest that the surface Pt atoms are strongly affected by the structure of the Ru and Pd substrates onto which the Pt is deposited, and, in the same line, that the Pt shell is uniformly formed, because the main Pt–Pt scattering cannot be observed up to the amount of Pt corresponding to Pt[1.0]/Ru and Pt[0.5]/Pd, respectively.

The coordination number provides us with useful information to depict the formation of a Pt shell during the reduction of Pt ions by HQ. The Pt–Pt coordination numbers (N) for samples

Table 1 ICP-AES results of Pd– and Ru–Pt core–shell nanoparticles with various ratios of Pt to Pd and Ru

Catalysts	[Pt]/[core] (at%)	Pt loading (wt%)	Total metal loading (wt%)
Pt[0.1]/Pd	11.3	5.6	32.3
Pt[0.3]/Pd	30.0	13.5	38.0
Pt[0.5]/Pd	51.8	21.2	43.6
Pt[0.7]/Pd	75.1	28.1	48.5
Pt[0.9]/Pd	92.4	32.5	51.6
Pt[0.2]/Ru	19.5	7.3	26.8
Pt[0.6]/Ru	58.5	19.2	36.2
Pt[1.0]/Ru	100.1	28.9	43.9
Pt[1.4]/Ru	137.4	35.8	49.3
Pt[1.6]/Ru	164.3	40.0	52.7

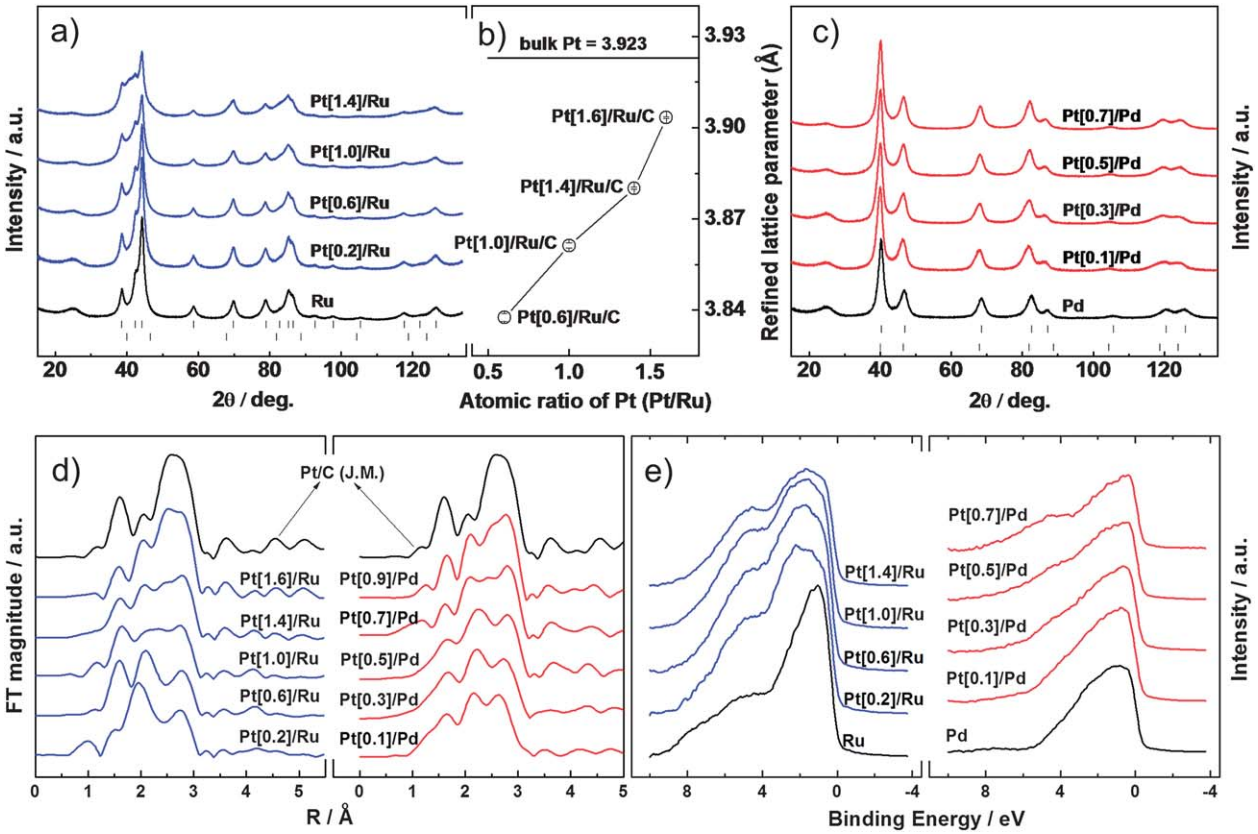

Fig. 3 Synchrotron X-ray measurements of Ru/C and Pd/C samples with various Pt loadings. (a) X-ray powder diffraction (PXRD) pattern for Ru and Ru–Pt samples. (b) Rietveld refined lattice parameters of Pt deposited on Ru/C. (c) PXRD patterns for Pd and Pd–Pt core–shell nanoparticle symbols in (a) and (c). (d) k^3-Weighted Fourier transform of Pt L_{III} EXAFS spectra for commercial Pt/C, Ru– (left) and Pd–Pt (right) core–shell nanoparticles with various loading amounts of Pt. (e) Valence band spectra for Ru and Ru–Pt (left), and Pd and Pd–Pt (right) core–shell nanoparticles obtained from X-ray photoelectron spectroscopy (XPS). The lines shown in (e) were smoothed using a five-points adjacent average on the background-subtracted XPS spectra.

with Pt/Pd ratios of 0.1 to 0.3 are smaller than those for pure Pt and core–shell samples with Pt loading higher than that of Pt [0.5]/Pd. On the other hand, the Pt–Pd coordination number presents an opposite behavior compared to the case of Pt–Pt, that is, it decreases with the increase of Pt loading. Similar trends were also observed for Ru–Pt core–shell nanoparticles (Table 2). This opposite trend between the coordination numbers (N) of Pt–Pt and Pt–Pd (Ru) indicates that Pt ions are reduced mainly on the surface of the core at early stage of Pt deposition (*i.e.*, up to Pt [0.5]/Pd and Pt[1.0]/Ru).

Table 2 Pt L_{III}-edge EXAFS structure parameters of Pd–Pt and Ru–Pt core–shell nanoparticles

	Pt–Pd (Ru)		Pt–Pt	
Catalysts	N^a	R^b/Å	N^a	R^b/Å
Pt/C (J.M.)	N/A	N/A	6.6 (5)	2.76 (1)
Pt[0.1]/Pd	2.2 (4)	2.70 (1)	3.0 (5)	2.68 (1)
Pt[0.3]/Pd	1.8 (2)	2.72 (1)	4.8 (7)	2.70 (1)
Pt[0.5]/Pd	1.7 (2)	2.74 (1)	6.0 (7)	2.73 (1)
Pt[0.7]/Pd	1.4 (1)	2.72 (1)	6.8 (7)	2.72 (1)
Pt[0.9]/Pd	1.1 (1)	2.73 (1)	6.4 (6)	2.74 (1)
Pt[0.2]/Ru	1.6 (5)	2.67 (2)	4.0 (7)	2.68 (2)
Pt[0.6]/Ru	1.6 (3)	2.70 (1)	3.4 (9)	2.71 (1)
Pt[1.0]/Ru	0.9 (2)	2.70 (3)	5.4 (8)	2.70 (3)
Pt[1.4]/Ru	1.0 (1)	2.71 (1)	6.3 (7)	2.72 (1)
Pt[1.6]/Ru	0.6 (1)	2.72 (2)	6.8 (8)	2.73 (1)

[a] Coordination number. [b] Interatomic Distance. The value in parenthesis denotes the estimated error of the calculated parameter.

As already reported in studies based on DFT calculations,[9,45,46] strained surface tends to shift the d-band center (ε_d) toward negative electron energy. In order to reveal the electronic modification induced by Pt deposition, surface electronic structures were obtained from high-resolution X-ray photoelectron spectroscopy (HR-XPS) at the 8A1 beamline of Pohang Accelerator Laboratory. The background-subtracted valence band spectra[3,38,44] of Ru–Pt (Fig. 3e, left) and Pd–Pt (Fig. 3e, right) nanoparticles are plotted for various Pt loadings. The position of ε_d for Ru nanoparticles with respect to the Fermi level shows a large difference compared to the theoretical value of Ru (−1.41 eV)[12] (Table 3). This may be attributed to a lack of efficient final-state screening from a carbon support[44] or a partial oxidation of surface Ru atoms. In contrast, Pd shows good agreement with the theoretical value of ε_d (−1.83 eV) (Table 3).[12,46] As the Pt loading increases a small feature centered at 4.7 eV, which is not observed for pure Pd, becomes apparent (Fig. 3e, right). A similar feature is also present in the Ru–Pt samples (Fig. 3e, left). Because of this higher binding energy feature, the estimated d-

Table 3 d-Band centers of Pd– and Ru–Pt core–shell nanoparticles

Pd–Pt		Ru–Pt	
Catalysts	d-Band center (eV)	Catalysts	d-Band center (eV)
Pd	−1.76	Ru	−2.42
Pt[0.1]/Pd	−1.88	Pt[0.2]/Ru	−2.81
Pt[0.3]/Pd	−1.88	Pt[0.6]/Ru	−2.83
Pt[0.5]/Pd	−2.05	Pt[1.0]/Ru	−2.92
Pt[0.7]/Pd	−2.05	Pt[1.4]/Ru	−2.86

band center from the measured spectra moved away from the Fermi edge with the increasing Pt loading. As expected, the observed d-band center shifts of the Pd–Pt samples upon Pt deposition are opposite to the shifts observed during Pd deposition on Pt(111) substrates.[44] The gradual shift to a higher binding energy (BE) strongly supports the assertion that Pt deposition occurs mainly on Pd (Ru) atoms in the surface layer. These results also prove that the electronic structure of the surface layer can be precisely controlled by varying the Pt loading.

Discussion on the HQ reduction method

For the uniform deposition of Pt on the surface of the preformed metallic particles the formation of a Pt shell onto the metal clusters should be favored compared to particle nucleation in the homogeneous phase or onto the carbon black particles. To favor the growth of a Pt overlayer, in this work, HQ was used as a mild reducing agent for Pt. The controlled deposition progresses by heating a solution containing Pt precursors, ethanol, HQ, and the preformed core nanoparticles, *i.e.*, carbon-supported Ru or Pd clusters.

As a control experiment the reduction of Pt by HQ was tested in the presence of carbon black. It confirmed that, even in the absence of a metal core, HQ can completely reduce Pt precursors. However, in this case only large Pt aggregates adsorbed onto the carbon black are present (Fig. 4). This explains a decreased nucleation probability of Pt onto carbon black compared to metal (Pd or Ru) clusters. On the other hand, once Pt nuclei are formed a further Pt deposition takes place more likely on these Pt nuclei compared to the bare carbon black substrate. Such a behavior supports the formation of large nanostructured Pt aggregates. Moreover, during filtering and washing Pt-loss was not detected proving that homogeneous nucleation of Pt did not take place in solution. Therefore, the control experiments support the hypothesis that, using the HQ reduction method, Pt ions are more easily deposited on preformed metal nanoparticles and that the probability to nucleate Pt on carbon black is low. This implies that the reduction is thermodynamically easier in the presence of a metal cluster as a support.

These findings are supported by cyclic voltammogram (CV) measurements made in an unbuffered aqueous electrolyte with HQ (0.1 M KNO_3 + 0.01 M 1,4-benzohydroquinone) on carbon black electrodes with and without Pt and Pd particles. These experiments permit us to study the probability of the nucleation and growth of Pt on carbon black during the HQ-assisted reduction process (Fig. 5). Anodic and cathodic peaks were observed at 0.67 V and 0.45 V, respectively; these are attributed to the well-known two-electron redox process.[27] These peaks have *ca.* 24–27 mV lower potential on metal nanoparticles compared to bare carbon black. It means that the presence of metal nanoparticles induces cathodic shifts of HQ oxidation. Therefore, the controlled weak reducing power of HQ has unique selectivity to the surface of preformed metal particles, and Pt ions are deposited mainly on the metal surface. Attractive interactions in the HQ-derived adlayer have also been reported.[40,41,42] The narrow width of the redox peak on Pt might be attributed to the formation of a compact arrangement of molecules in the adlayer.

Oxygen reduction activity of core–shell electrocatalysts

The electrocatalytic properties of the core–shell nanoparticles were benchmarked against commercial Pt/C (40 wt%, Johnson-Matthey). Fig. 6a and S4 (ESI†) display polarization curves of the ORR on commercial Pt and the core–shell nanoparticles supported on carbon black. As expected, the overpotentials decreased with Pt loadings. More precisely, the half-wave potentials of Pt/C (40 wt%, Johnson-Matthey), Pt[0.1], Pt[0.3], Pt[0.5], Pt[0.7], and Pt[0.9]/Pd/C were 897, 854, 901, 914, 918, and

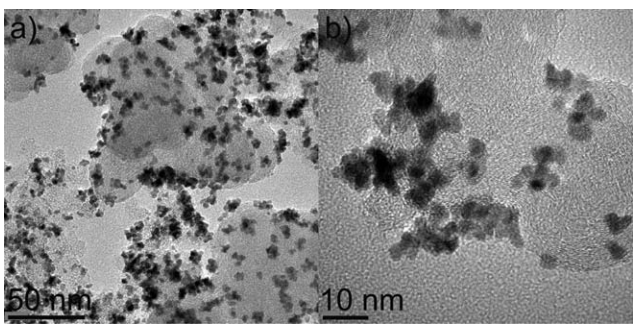

Fig. 4 TEM images of Pt/C (31.8 wt%) prepared by hydroquinone reduction. Magnification of (a) 88 000 and (b) 255 000.

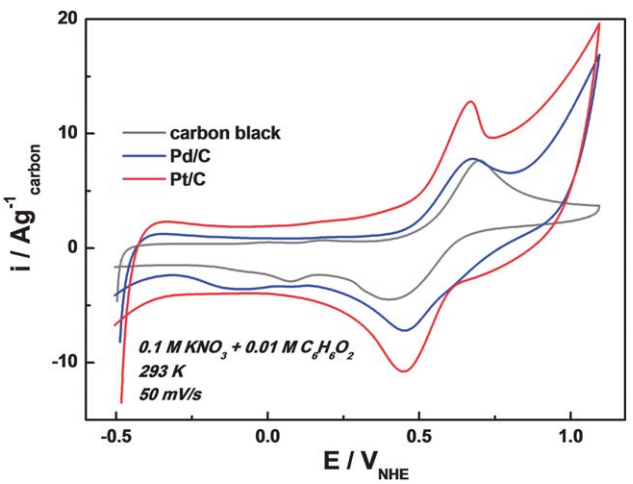

Fig. 5 Comparison of the redox behaviors of hydroquinone on different electrode materials. First scans of cyclic voltammograms recorded for 0.01 M HQ (1,4-benzohydroquinone) in 0.1 M KNO_3 on carbon black, Pd/C, and commercial Pt/C (40 wt%) electrodes.

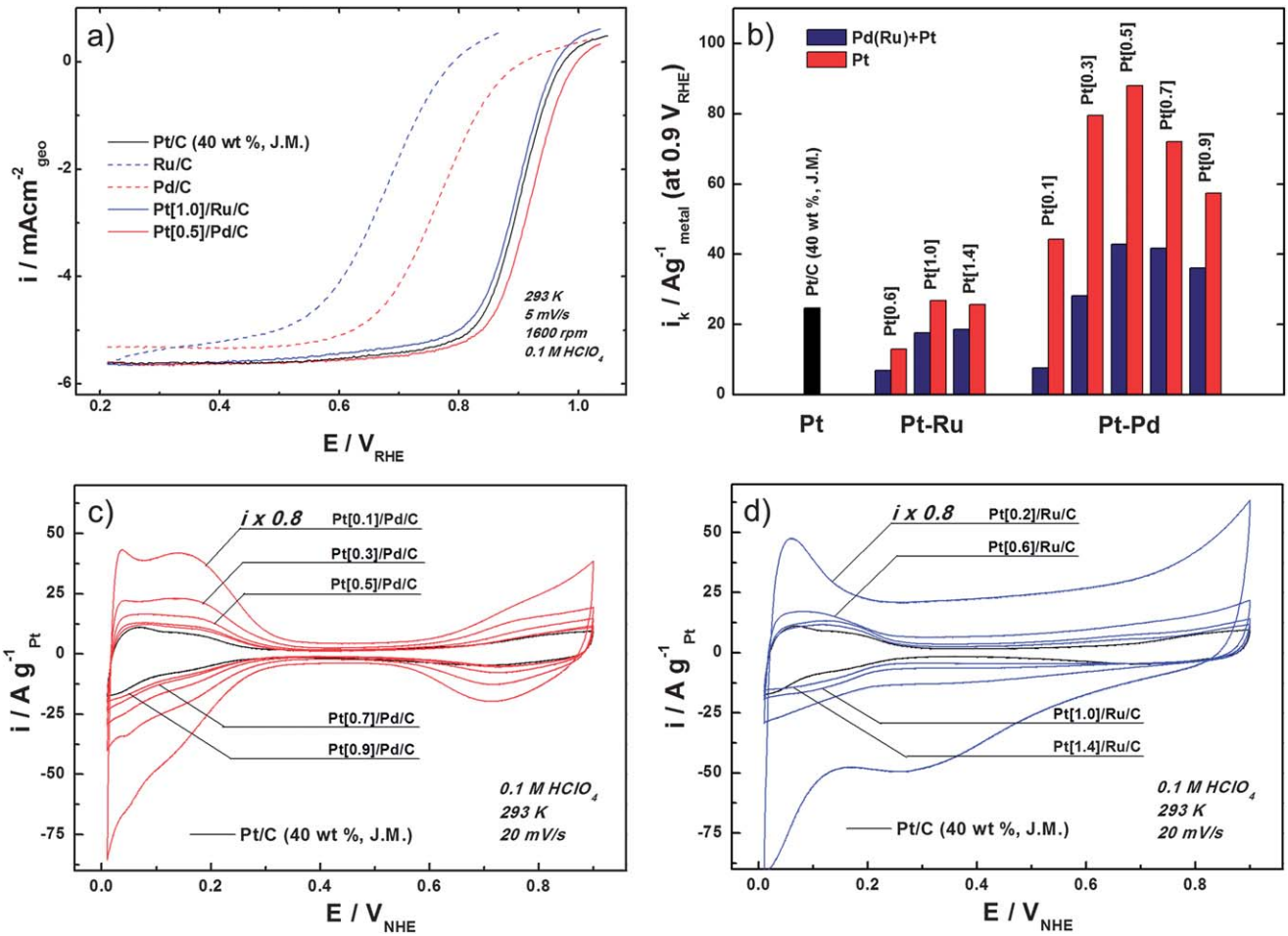

Fig. 6 Electrochemical characterization of Pd– and Ru–Pt core–shell nanoparticles. (a) Comparison of polarization curves for the O_2 reduction reaction on commercial Pt/C (40 wt%, Johnson-Matthey), core, and core–shell nanoparticles. (b) Mass-specific activity at 0.9 V *vs.* RHE for these core–shell catalysts. Mass-specific activity is given as a kinetic current density i_k that is normalized in reference to the loading amount of Pt. Cyclic voltammograms of (c) Pd–Pt and (d) Ru–Pt core–shell nanoparticles. Currents were normalized to the loading amount of Pt. Currents of Pt[0.2]/Ru/C and Pt[0.1]/Pd/C are multiplied by 0.8.

916 mV (*vs.* RHE), respectively (Fig. S4†). Starting from a Pt loading of Pt : Pd = 0.3 : 1 (Pt[0.3]/Pd/C), Pd–Pt nanoparticles showed lower overpotentials than the commercial Pt/C (0.897 V *vs.* RHE). The half-wave potentials are almost the same between Pt loadings from Pt[0.5]/Pd to Pt[0.9]/Pd. It is in excellent agreement with the same and slightly different ε_d values of Pd–Pt (Pt[0.5]/Pd and Pt[0.7]/Pd) and Ru–Pt (Pt[1.0]/Ru and Pt[1.4]/Ru) core–shell nanoparticles, respectively. This good agreement between electrochemical activity and electronic modification strongly suggests that the Pt atoms added above Pt[0.5]/Pd are deposited mainly onto surface Pt rather than the exposed surface Pd. Furthermore, they cause the disappearance of the electronic modification by substrates, *i.e.*, metal cores. Pt[0.7]/Pd showed the highest half-wave potentials (Fig. S4†). In the case of the Pt/Ru/C samples, the half-wave potentials of Pt[0.2], Pt[0.6], Pt[1.0], and Pt[1.4]/Ru were 727, 851, 889, and 899 mV (*vs.* RHE), respectively.

Pt[0.5]/Pd/C and Pt[1.0]/Ru/C exhibited a dramatic increase of the half-wave potentials relative to the corresponding core nanoparticles (Fig. 6a and S4†). The main difference between Ru–Pt and Pd–Pt consists of the much higher ORR activity of the latter system. It is noteworthy that the ratio of Pt : Ru = 1.4 : 1 (Pt[1.4]/Ru/C) had a slightly higher ORR activity than the commercial Pt/C. Ru core particles required higher Pt loading than that of the Pd–Pt system in order to display an activity comparable to the commercial Pt/C because of the large down-shift of the d-band center of Pt by Ru substrate[4] (*cf.* also Table 3).

The kinetic current (i_k) was calculated by the Koutecky–Levich equation and normalized in reference to the metal loading (Fig. 6b). The mass-specific activity reached a maximum value for the Pt : Pd = 0.5 : 1 (Pt[0.5]/Pd/C) and did not increase further with the increase of Pt loading. At 0.9 V, the ORR activity of Pt[0.5]/Pd/C (21.2 wt% loading of Pt, Table 1) was enhanced by factors of 1.74 and 3.57 relative to Pt/C (40 wt%, Johnson-Matthey) on the basis of the mass of all metals and Pt only, respectively. Ru–Pt core–shell nanoparticles also showed enhanced activity, *i.e.*, the mass-specific activity and half-wave potential of Pt[1.4]/Ru/C (35.8 wt% loading of Pt, *cf.* Table 1) had slightly higher values than the commercial Pt/C (Fig. 6b).

Fig. 6c and d show cyclic voltammograms (CVs) of the Pd–Pt and Ru–Pt samples in 0.1 M $HClO_4$ at a scan rate of 20 mV s^{-1}. Current densities were normalized to Pt loading in order to

compare the mass-specific active surface areas of different electrocatalysts. The area of the H_{upd} region normalized to the Pt mass decreases with the amount of Pt, because an increase of Pt loading results in a decrease in the electrochemically active surface sites (Pt and Pd) per unit mass of Pt. For example, the mass-specific active area of Pt[0.5]/Pd/C (64.8 $m^2\ g_{Pt}^{-1}$) is 180% higher than the one of commercial Pt/C (36.0 $m^2\ g_{Pt}^{-1}$). Ru–Pt shows a similar trend as the Pd–Pt nanoparticles (Fig. 6d). It should also be noted that an increase of the Pt loading resulted in a significant decrease in the double layer capacitance, which is known to be caused by RuO_x species.[47] This clearly indicates that the exposed Ru atoms are almost completely covered by Pt, further supporting the core–shell structural model.

Conclusions

The Pt precursor is preferentially reduced at the metal surface through the hydroquinone reduction method, and it forms a Pt overlayer as a result of the unique selectivity and the high redox potential of hydroquinone. We demonstrated, from TEM and various synchrotron X-ray analyses, that the Ru–Pt and Pd–Pt nanoparticles have the geometric and electronic characteristics of core–shell nanocrystallites.

The ORR activity of Pt[0.5]/Pd/C (21.2 wt% loading of Pt) was enhanced by a factor of 1.74 and 3.57 relative to commercial Pt/C (40 wt%) at 0.9 V *vs.* RHE on the basis of the mass of all metals and Pt, respectively. The valence band spectra obtained from HR-XPS reflect that the enhancement in the ORR activity can be mainly attributed to the modification of the Pt d-band properties due to the electronic interaction of Pt with the core metal. Finally, the oxidation reaction of hydroquinone in ethanol at an elevated temperature occurs preferentially on the surface of metal clusters even in the presence of a carbon support. Consequently, the hydroquinone reduction method brings a novel chemical route for the preparation of real electrocatalysts with low costs and high activities for fuel cells.

Acknowledgements

This research was supported by WCU (World Class University) program through the National Research Foundation of Korea funded by the Ministry of Education, Science and Technology (R31-10013).

Notes and references

1 J. A. Rodriguez and D. W. Goodman, *Science*, 1992, **257**, 897.
2 J. K. Nørskov, T. Bligaard, J. Rossmeisl and C. H. Christensen, *Nat. Chem.*, 2009, **1**, 37.
3 V. R. Stamenkovic, B. Fowler, B. S. Mun, G. F. Wang, P. N. Ross, C. A. Lucas and N. M. Markovic, *Science*, 2007, **315**, 493.
4 J. Greeley, I. E. Stephens, A. S. Bondarenko, T. P. Johansson, H. A. Hansen, T. F. Jaramillo, J. Rossmeisl, I. Chorkendorff and J. K. Nørskov, *Nat. Chem.*, 2009, **1**, 552.
5 M. R. Tarasevich, A. Sadkowski and E. Yeager, Oxygen Electrochemistry, in *Comprehensive Treatise of Electrochemistry*, ed. B. E. Conway, J.O'M. Bockris, E. Yeager, S. U. M. Khan and R. E. White, Plenum Press, New York, 1983, vol. 7, p. 301.
6 J. Zhang, K. Sasaki, E. Sutter and R. R. Adzic, *Science*, 2007, **315**, 220.
7 J. Greeley and J. K. Nørskov, *Electrochim. Acta*, 2007, **52**, 5829.
8 J. X. Wang, H. Inada, L. J. Wu, Y. M. Zhu, Y. M. Choi, P. Liu, W. P. Zhou and R. R. Adzic, *J. Am. Chem. Soc.*, 2009, **131**, 17298.
9 J. L. Zhang, M. B. Vukmirovic, Y. Xu, M. Mavrikakis and R. R. Adzic, *Angew. Chem., Int. Ed.*, 2005, **44**, 2132.
10 F. H. B. Lima, J. Zhang, M. H. Shao, K. Sasaki, M. B. Vukmirovic, E. A. Ticianelli and R. R. Adzic, *J. Phys. Chem. C*, 2007, **111**, 404.
11 J. Greeley and J. K. Nørskov, *J. Phys. Chem. C*, 2009, **113**, 4932.
12 A. Ruban, B. Hammer, P. Stoltze, H. L. Skriver and J. K. Nørskov, *J. Mol. Catal. A: Chem.*, 1997, **115**, 421.
13 B. Hammer and J. K. Nørskov, *Adv. Catal.*, 2000, **45**, 71.
14 V. Stamenkovic, B. S. Mun, K. J. J. Mayrhofer, P. N. Ross, N. M. Markovic, J. Rossmeisl, J. Greeley and J. K. Nørskov, *Angew. Chem., Int. Ed.*, 2006, **45**, 2897.
15 J. K. Nørskov, J. Rossmeisl, A. Logadottir, L. Lindqvist, J. R. Kitchin, T. Bligaard and H. Jonsson, *J. Phys. Chem. B*, 2004, **108**, 17886.
16 J. Rossmeisl, A. Logadottir and J. K. Nørskov, *Chem. Phys.*, 2005, **319**, 178.
17 F. Abild-Pedersen, J. Greeley, F. Studt, J. Rossmeisl, T. R. Munter, P. G. Moses, E. Skulason, T. Bligaard and J. K. Nørskov, *Phys. Rev. Lett.*, 2007, **99**, 106105.
18 J. Turkevich, R. S. Miner and L. Babenkova, *J. Phys. Chem.*, 1986, **90**, 4765.
19 G. Schmid, A. Lehnert, J. O. Malm and J. O. Bovin, *Angew. Chem., Int. Ed. Engl.*, 1991, **30**, 874.
20 Y. Wang and N. Toshima, *J. Phys. Chem. B*, 1997, **101**, 5301.
21 S. E. Habas, H. Lee, V. Radmilovic, G. A. Somorjai and P. Yang, *Nat. Mater.*, 2007, **6**, 692.
22 S. Alayoglu, A. U. Nilekar, M. Mavrikakis and B. Eichhorn, *Nat. Mater.*, 2008, **7**, 333.
23 V. K. LaMer and R. H. Dinegar, *J. Am. Chem. Soc.*, 1950, **72**, 4847.
24 F. Xie, M. S. Baker and E. M. Goldys, *J. Phys. Chem. B*, 2006, **110**, 23085.
25 S. D. Perrault and W. C. W. Chan, *J. Am. Chem. Soc.*, 2009, **131**, 17042.
26 M. Quan, D. Sanchez, M. F. Wasylkiw and D. K. Smith, *J. Am. Chem. Soc.*, 2007, **129**, 12847.
27 M. E. Peover, *J. Chem. Soc.*, 1962, 4540.
28 M. Gupta and H. Linschitz, *J. Am. Chem. Soc.*, 1997, **119**, 6384.
29 T.-Y. Jeon, N. Pinna, S. J. Yoo, S.-H. Yu, S.-K. Kim, S. Lim, D.-H. Peck, D.-H. Jung and Y.-E. Sung, *J. Electroanal. Chem.*, 2011, **662**, 70.
30 N. Krishnankutty, J. Li and M. A. Vannice, *Appl. Catal., A*, 1998, **173**, 137.
31 M. Bowker, J. Counsell, K. El-Abiary, L. Gilbert, C. Morgan, S. Nagarajan and C. S. Gopinath, *J. Phys. Chem. C*, 2010, **114**, 5060.
32 T.-Y. Jeon, S. J. Yoo, H.-Y. Park, S.-K. Kim, S. Lim, D. Peck, D.-H. Jung and Y.-E. Sung, *Langmuir*, 2012, **28**, 3664.
33 Whole-pattern profile matching was carried out using FULLPROF program, J. Rodrguez-Carvajal, *Abstracts of the Satellite Meeting on Powder Diffraction of the XV Congress of the IUCr*, Toulouse, France, 1990, p. 127.
34 B. Ravel and M. Newville, *J. Synchrotron Radiat.*, 2005, **12**, 537.
35 A. L. Ankudinov, B. Ravel, J. J. Rehr and S. D. Conradson, *Phys. Rev. B: Condens. Matter Mater. Phys.*, 1998, **58**, 7565.
36 S. Siegel, R. H. Henry and S. T. Benjamin, *J. Inorg. Nucl. Chem.*, 1969, **31**, 3803.
37 J. S. Kasper and K. Lonsdale, *International Tables for X-ray Crystallography*, V.3. D. Reidel Pub. Co., 1985.
38 W. P. Zhou, A. Lewera, R. Larsen, R. I. Masel, P. S. Bagus and A. Wieckowski, *J. Phys. Chem. B*, 2006, **110**, 13393.
39 M. C. Daniel and D. Astruc, *Chem. Rev.*, 2004, **104**, 293.
40 S. T. Gentry, S. J. Fredericks and R. Krchnavek, *Langmuir*, 2009, **25**, 2613.
41 M. Rodriguez-Lopez, A. Rodes, E. Herrero, P. Tunon, J. M. Feliu, A. Aldaz and A. Carrasquillo, *Langmuir*, 2009, **25**, 10337.
42 M. Rodriguez-Lopez, E. Herrero, J. M. Feliu, P. Tunon, A. Aldaz and A. Carrasquillo, *J. Electroanal. Chem.*, 2006, **594**, 143.
43 J. Zhang, F. H. B. Lima, M. H. Shao, K. Sasaki, J. X. Wang, J. Hanson and R. R. Adzic, *J. Phys. Chem. B*, 2005, **109**, 22701.
44 Rietveld refinement was carried out using FullProf, J. Rodriguez-Carvajal, *Abstracts of the Satellite Meeting on Powder Diffraction of the XV Congress of the IUCr*, Toulouse, France, 1990, p. 127.
45 B. S. Mun, C. Lee, V. Stamenkovic, N. M. Markovic and P. N. Ross, *J. Chem. Phys.*, 2005, **122**, 184712.
46 J. Greeley and M. Mavrikakis, *Nat. Mater.*, 2004, **3**, 810.
47 G. Wu, L. Li and B. Q. Xu, *Electrochim. Acta*, 2004, **50**, 1.